High-pressure lithium as an elemental topological semimetal

S. F. Elatresh,[1] Zhimou Zhou,[2] N. W. Ashcroft,[3] S. A. Bonev,[4,*] Ji Feng,[2,5,6,†] and Roald Hoffmann[1,‡]

[1]*Department of Chemistry and Chemical Biology, Cornell University, Baker Laboratory, Ithaca, New York 14853-1301, USA*

[2]*International Center for Quantum Materials, School of Physics, Peking University, Beijing 100871, China*

[3]*Laboratory of Atomic and Solid State Physics, Cornell University, Ithaca, New York 14853-1301, USA*

[4]*Lawrence Livermore National Laboratory, Livermore, California 94550, USA*

[5]*Collaborative Innovation Center of Quantum Matter, Beijing 100871, China*

[6]*CAS Center for Excellence in Topological Quantum Computation, University of Chinese Academy of Sciences, Beijing 100190, China*

(Received 1 February 2019; published 23 April 2019)

Topological semimetals generally contain heavy elements. Using density-functional theoretic calculations, we predict that three dense lithium polymorphs in the pressure range 200–360 GPa display nontrivial semimetallic electronic structure. Specifically, these high-pressure phases exhibit Fermi pockets which are degenerate over a loop in $\boldsymbol{k}$ space, around which an encircling $\boldsymbol{k}$-space path is threaded by $\pm\pi$ Berry phase. Accordingly, these dense lithium phases are topological nodal loop semimetals involving a single light element.

DOI: 10.1103/PhysRevMaterials.3.044203

I. INTRODUCTION

Pressure can induce dramatic changes to a material's geometric and electronic structures, resulting in highly complex chemical and physical behavior. At ambient pressure, the light alkali metals, such as lithium and sodium, are viewed as simple metals; the nearly-free electron approximation picture adequately describes their valence electrons. However, the phase diagrams of Li and Na are riddled with novel features, which are clearly nonsimple [1–12]. Lithium, in particular, patently departs from the realm of simple metals under the application of external pressure.

At ambient pressure and temperature, lithium is a good metal forming a simple and highly symmetric body-centered-cubic (bcc) crystal structure. As the pressure is increased, starting near 40 GPa, it undergoes several transformations to complex low-symmetry phases. The structural changes are coupled to counterintuitive modifications of its electronic properties, which cannot be explained by a theory based on the nearly-free-electron approximation. A number of exotic high-pressure phenomena ensue, including a metal-to-semiconductor transition, reappearance of metallization, superconductivity, anomalous melting curve, and electride properties [2,6,7,10,13–19].

Clearly, these changes must be accompanied by nontrivial electronic band structure modifications. Most of the previous studies on the electronic properties of dense solid lithium have focused on the metal-to-semiconductor transition found around 80 GPa pressure [17] and on its superconducting properties from 35 to 48 GPa [20–25] and beyond [26]. At higher pressures and low temperature, the research to date has mainly focused on determining the preferred Li crystal structures [14,27]. It has been shown that the high-pressure phases are characterized with the appearance in the electron band structure of a pseudogap, *s*-to-*p* charge transfer, and electridelike localization of the conduction electrons in interstitial ionic regions [14,19,27–29]. However, the possibility for reappearing semiconducting behavior or the emergence of states with no-trivial topology has not been examined in detail.

Topologically nontrivial metals and semimetals have been the focus of much interest in modern condensed matter physics research. Their electronic structures exhibit nontrivial band crossings near the Fermi energy, around which the low-energy excitations behave differently from the conventional Schrödinger-type fermions. For example, Weyl and Dirac semimetals host isolated twofold and fourfold degenerate points, respectively, with linear energy dispersions. Their electronic excitations are analogous to the relativistic Weyl and Dirac fermions [30–34], making it possible to simulate interesting high-energy physics phenomena in condensed matter systems [35]. Most materials studied either consist of binary compounds of heavy elements, such as Cd_3As_2 [32] and Na_3Bi [31,33], or are still more complex compounds [36]. Although some Dirac-like features have been observed in the band structures of lithium subhydrides under pressure [37] and predicted for dense hydrogen surface states [38], topological semimetals involving only a single light element are hitherto unknown [39].

In this work, we report a first-principles study on the lightest metallic element, lithium, under high pressure ranging from 200 to 360 GPa. We focus on the three stable phases in this pressure range, namely, those with space groups *Cmca*-24, *Cmca*-56, and $P4_2/mbc$. We find that in all these phases, high pressure tends to drive the valence electrons to localize in the interstitials of the rather complex Li networks. We also show that their electronic structures share some common features. Importantly, all of these three phases turn out to be topological nodal-loop semimetals. If

*bonev@llnl.gov
†jfeng11@pku.edu.cn
‡rh34@cornell.edu

the predictions for dense lithium made here are confirmed by experiments, lithium would be the simplest and lightest three-dimensional (3D) topological nodal-loop semimetal material discovered.

II. COMPUTATIONAL METHODS

Full structural optimization, enthalpy, electronic band structure, and density of states calculations were performed within density-functional theory (DFT) using the ABINIT code [40] with three-electron Hartwigsen-Goedeker-Hutter pseudopotential [41], and the generalized gradient approximation parametrized by Perdew, Burke, and Ernzerhof (GGA-PBE) [42]. A plane-wave expansion with a 2700 eV cutoff and a **k**-point grid for self-consistent calculations as large as $10 \times 10 \times 10$, $6 \times 6 \times 6$, and $16 \times 16 \times 16$ were used for *Cmca*-24, *Cmca*-56, and $P4_2/mbc$, respectively. These dense **k**-point grids are sufficient to ensure convergence for enthalpies to better than 1 meV/atom.

For the rest of the analysis, DFT calculations were performed using the Vienna *ab initio* simulation package (VASP), within GGA-PBE [42,43]. The Kohn-Sham states were expanded in the plane-wave basis set with a kinetic energy truncation at 900 eV. In self-consistent calculations, to obtain a converged Brillouin zone summation, $9 \times 9 \times 9$, $7 \times 7 \times 15$, and $9 \times 9 \times 9$ $\boldsymbol{k}$ grids centered at the Γ point were applied for *Cmca*-24, *Cmca*-56, and $P4_2/mbc$, respectively. To calculate the Fermi surface at a sufficiently dense $\boldsymbol{k}$ grid but at a relatively low computation cost, we employ the Wannier interpolation method as implemented in Ref. [44]. We verified that the band structures and density of states obtained with VASP agree with those from ABINIT.

III. RESULTS

A. Crystal structure

The relative enthalpies of the *Cmca*-24, *Pbca*, *Cmca*-56, and $P4_2/mbc$ structures in the pressure range from 50 to 500 GPa are shown in Fig. 1. These results are consistent with previous calculations [11,14,27] and experimental data [10,11]. Space group *Pbca* is a maximal subgroup of *Cmca*. As pressure is increased, the parameters of the optimized *Pbca* structure (space group no. 61; 24-atom primitive cell) evolve and by 95 GPa it converges to *Cmca*-24 (space group no. 64; 12-atom primitive cell) (see Fig. S15 for an x-ray diffraction comparison of the two phases below and above 95 GPa). The *Cmca*-24 structure (and its equivalent *Pbca*) remains preferred until 226 GPa in agreement with previous calculations [14,27]. Above 226 GPa, *Cmca*-56 (28-atom primitive cell) has the lowest enthalpy and remains such until about 320 GPa. At higher pressure, *Cmca*-56 becomes unfavorable with respect to $P4_2/mbc$. While there have been some disagreements for the exact transition pressures between these phases [11,14,27,45], they are of little consequence for the conclusions of the present work. The findings reported in what follows for each structure persist over relatively large pressure ranges. We have therefore selected a single pressure for each structure, well within their stability regions, to analyze their electronic properties.

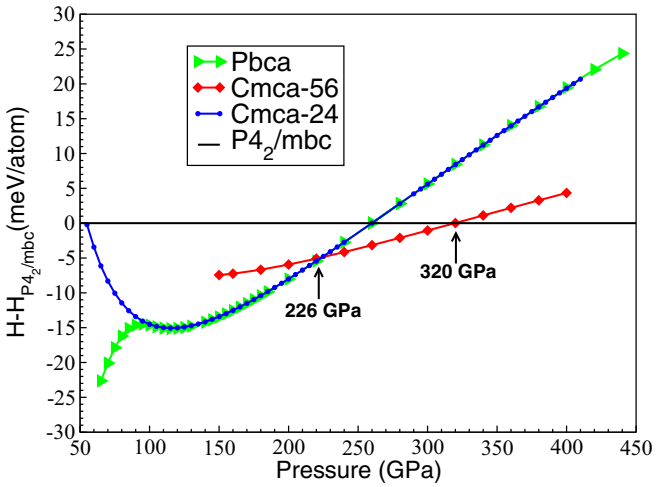

FIG. 1. Enthalpies of the most competitive lithium structure computed relative to the $P4_2/mbc$ structure.

B. Electronic band structure

The electronic band structures and densities of states of the three lithium structures were computed at selected pressures within their regions of stability. The results are shown in Fig. 2. The band structures in all three phases show similar Dirac-like characteristics and semimetal behavior. Specifically, the valence and conduction bands touch each other near the Γ, *Y*, and *Z* symmetry points for *Cmca*-24, *Cmca*-56, and $P4_2/mbc$ phases, respectively. The electronic densities of states of all three structures are greatly diminished at the Fermi level, however, remain finite. Since the GGA is known to underestimate the electronic band gap, we have carried out hybrid exchange band structure calculations within the Heyd-Scuseria-Ernzerhof approximation (HSE06) [46] as implemented in VASP [43,47], with otherwise exactly the same simulation parameters as in the GGA-PBE calculations. The HSE06 results confirm that the dense lithium phases retain their semimetal behavior [see Fig. S6(b) for the HSE06 band structure of $P4_2/mbc$ at 360 GPa].

The semimetal behavior can be further illustrated by Fermi surface plots, as shown in Fig. 3. Here we see very small Fermi surface patches, which indicates that the band crossing points are rather near the Fermi level.

In order to better ascertain the nature of the degeneracies in these high-pressure lithium phases, we have constructed Wannier functions for band interpolation [48] for these phases. In Fig. 3, we show the Wannier functions of all three phases at selected pressures within their stability ranges; these reveal very peculiar localization of the valence electrons. The Li atoms are depicted as pink spheres. The isosurfaces of Wannier functions are drawn as blue-colored surfaces. For clarity, only one of the Wannier functions for each structure is drawn in Fig. 3. It can be clearly seen that the Wannier wave functions are localized in the interstitials of the rather complex Li networks. The strong interstitial localization is again a manifestation of the exclusionary effect of ionic cores in compressed phases [49]. The localization of electrons can also be seen through electron localization functions (see Fig. S10 for details [50]). As the electrons are localized in the

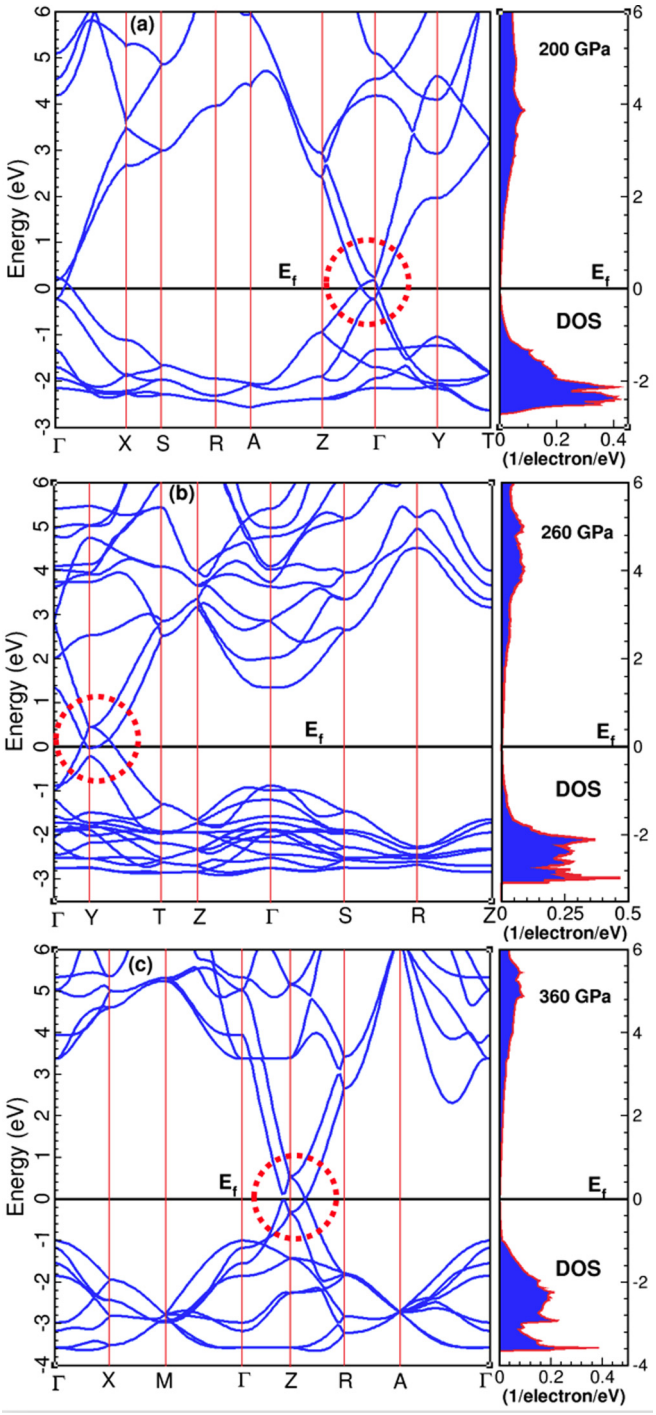

FIG. 2. Calculated electronic band structures and density of states of Li (a) *Cmca*-24 structure at 200 GPa, (b) *Cmca*-56 at 260 GPa, and (c) $P4_2/mbc$ at 360 GPa.

interstitials, these phases can be thought of as elemental electrides, Li^+e^- [51].

C. Nodal loops

From the calculated band structures and density of states shown in Fig. 2, all three phases are semimetals, with valence and conduction bands touching at some momenta in the respective Brillouin zones. The degeneracies uncovered above

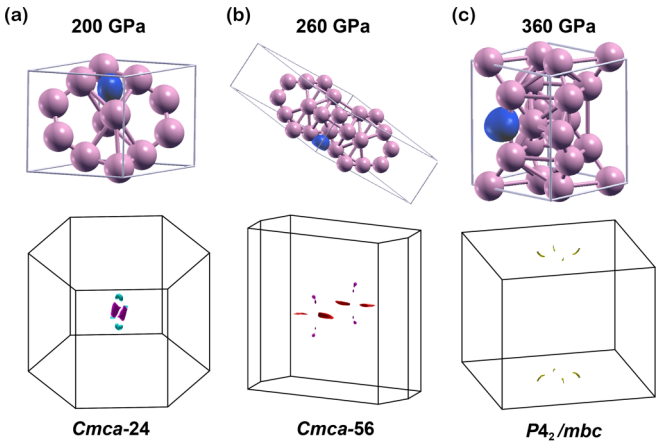

FIG. 3. 3D illustrations of the Li crystal structure unit cells and Fermi surfaces. The blue balls are isosurface plots of one of the Wannier functions which show electron localization in the interstitials. (a) *Cmca*-24 phase at 200 GPa. (b) *Cmca*-56 at 260 GPa, and (c) $P4_2/mbc$ at 360 GPa.

may point to topological semimetals, such as Dirac or Weyl semimetals. However, it is noted that the inclusion of spin-orbit coupling in the calculations incurs little changes to the band structure, as expected from the lightness of lithium element. Thus, if these degeneracies assumed Dirac-type linear dispersion, the electronic structure would correspond to Weyl semimetals. On the other hand, the presence of time-reversal and inversion symmetry in all three phases precludes such possibility, as at least one of the two symmetries must be broken in a Weyl semimetal. These analyses then leave us with the interesting possibility of nodal line semimetals.

Therefore, it is essential to scrutinize the band crossings in detail, which is made possible by expedient band interpolation via Wannier functions. We plot the dispersions of valence and conduction bands in two-dimensional $\boldsymbol{k}$ planes and along lines in the $\boldsymbol{k}$ space. The results are shown in Fig. 4. It can be clearly seen that for the *Cmca*-24 phase there are two Dirac-like points along the $\boldsymbol{b}_3$ axis, located at $\boldsymbol{k} = (0, 0, \pm 0.13)$ [see Fig. 5(a)] about 50 meV above the Fermi level. Meanwhile, the energy dispersions in the $k_y = 0$ plane [Fig. 4(b)] exhibit four Dirac-like cones, indicating extra degeneracies. Actually, there are two nodal loops in the $k_z = 0$ and $k_x = -k_y$ planes where valence and conduction bands cross each other [see Figs. 5(a) and S8 [50]). The situation for the *Cmca*-56 phase is similar to that in *Cmca*-24. There are two Dirac-like points located at the boundary of the Brillouin zone with $\boldsymbol{k} = (0.5, 0.5, \pm 0.12)$ [Fig. 5(b)], almost on the Fermi level, as shown in Fig. 4(c). The degenerate nodal loops are located in the $k_z = 0$ and $k_x = -k_y$ planes [see Figs. 5(b) and S9 [50]]. The center of the nodal loops shifts to the boundary of the Brillouin zone (Y). The $P4_2/mbc$ phase, however, is slightly different. There are two degenerate nodal loops in the $k_x = 0$ and $k_y = 0$ planes [see Figs. 5(c) and S10 for details [50]]. The center of the nodal loops is located at the boundary of the Brillouin zone (Z). The crossing points between the nodal loops and the $k_z = 0.5$ plane are $(\pm 0.13, 0, 0.5)$ and $(0, \pm 0.13, 0.5)$, as shown in Fig. 4(e). The locations of the

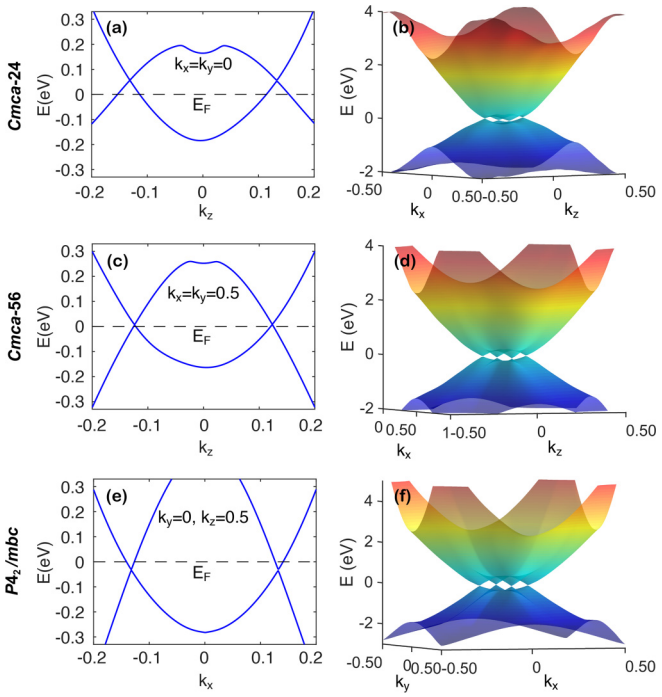

FIG. 4. Calculated valence and conduction energy bands along (a) $k_x = k_y = 0$ for the *Cmca*-24 phase at 200 GPa, (c) $k_x = k_y = 0.5$ for *Cmca*-56 at 260 GPa, and (e) $k_y = 0$, $k_z = 0.5$ for $P4_2/mbc$ at 360 GPa. (b), (d), and (f) are energy dispersion surfaces in the $k_y = 0$ plane for the *Cmca*-24, $k_y = 0.5$ for *Cmca*-56, and $k_z = 0.5$ for $P4_2/mbc$, respectively.

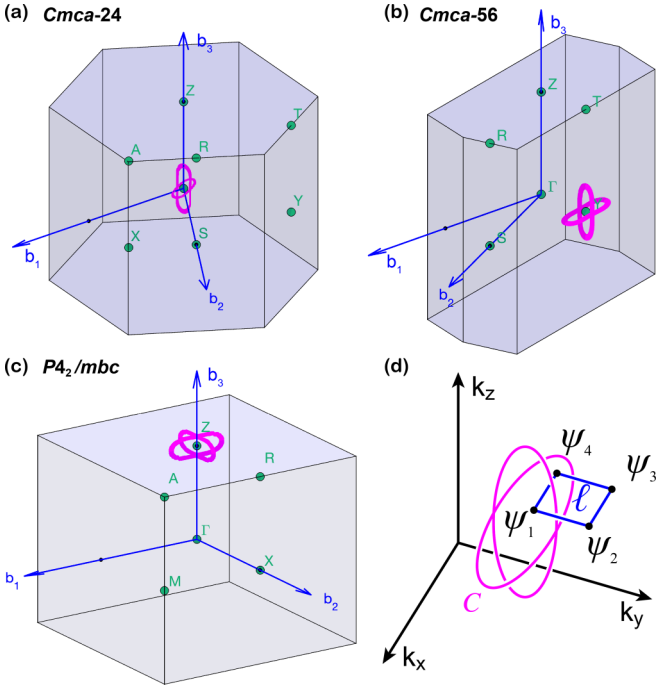

FIG. 5. Brillouin zones, degenerate nodal loops (magenta curves) for the *Cmca*-24 (a), *Cmca*-56 (b), and $P4_2/mbc$ (c) phases. High-symmetry points are denoted by green points. (d) An example of the closed path ℓ (blue rectangle) that encircles the nodal loop C (magenta loop).

degenerate nodal loops within the Brillouin zone of each structure are shown in Fig. 5.

The nodal loops in all these phases are protected by either the $\mathcal{PT}$ symmetry or the glide mirror symmetries. Without spin-orbit coupling, the existence of nodal loop C under $\mathcal{PT}$ symmetry requires that the Berry phase for any closed path ℓ encircling the loop C is $\pm\pi$ [52]. We pick four $\boldsymbol{k}$ points encircling the candidate nodal lines and compute the Berry phase by summing the Berry connections, as depicted in Fig. 5(d). The Berry phase is given by

$$\gamma_\ell = \sum_{n\in \text{occ.}} \oint_\ell \langle u_n(\boldsymbol{k})|i\nabla_{\boldsymbol{k}} u_n(\boldsymbol{k})\rangle d\boldsymbol{k},$$
$$= -\,\text{tr Im log}\, \psi_1^\dagger \psi_2 \psi_2^\dagger \psi_3 \psi_3^\dagger \psi_4 \psi_4^\dagger \psi_1, \qquad (1)$$

where $|u_n(\boldsymbol{k})\rangle$ is the periodic part of the Bloch eigenstates and the summation is over all occupied states. The second equality is used in numerical evaluation of the spinless Berry phase, in which $\psi_i = (|u_1(\boldsymbol{k}_i)\rangle, |u_2(\boldsymbol{k}_i)\rangle, \ldots, |u_M(\boldsymbol{k}_i)\rangle)$, and M is the number of occupied states. A nontrivial Berry phase will protect the nodal loop against weak perturbations from gap opening. According to our numerical calculations based on tight-binding Hamiltonians, all three of these phases yield nontrivial Berry phases ($\pm\pi$) for closed paths encircling the nodal loops. The presence of glide mirror symmetries will further pin the nodal loops to corresponding planes in the momentum space, as specified in Fig. 5.

To further examine and characterize the nature of the degeneracies in these high-pressure lithium phases, we construct and analyze an effective $\boldsymbol{k}\cdot\boldsymbol{p}$ Hamiltonian. Here we take the tetragonal phase ($P4_2/mbc$) as an example. We construct a two-band model for the valence and conduction bands. To capture the degenerate nodal loops we expand the Hamiltonian at the $Z = (0, 0, 1/2)$ point of the Brillouin zone. Considering the $C_2(z)$ symmetry, we let $\tilde{k}_z \equiv k_z - 0.5$, and the Hamiltonian is written as

$$H(\boldsymbol{k}) = \sum_{i=0}^{3} h_i \sigma^i, \qquad (2)$$

where σ^i are Pauli matrices, and h_i are quadratic functions of $\boldsymbol{k}$ determined by the symmetry of Z, $i = 0, 1, 2, 3$. Specifically, $h_2 = 0$, $h_i = a_i + b_i\tilde{k}_z + c_i k_x^2 + d_i k_y^2 + e_i\tilde{k}_z^2$ for $i = 0$ and 3, and $h_1(k_x, k_y, \tilde{k}_z) = f k_x k_y$. The eigenvalues of Eq. (2) are given by

$$\varepsilon_\pm(\boldsymbol{k}) = h_0 \pm \sqrt{h_1^2 + h_3^2}. \qquad (3)$$

It can be clearly seen that the valence and conduction bands will touch each other provided that $h_1 = h_3 = 0$. In the

TABLE I. Fitted parameters for the $\boldsymbol{k}\cdot\boldsymbol{p}$ Hamiltonian for the $P4_2/mbc$ phase in Eq. (2) in units of eV.

a_0	b_0	c_0	d_0	e_0	f
0.053	0.002	−5.106	−4.921	−11.210	−89.398
a_3	b_3	c_3	d_3	e_3	
−0.317	−0.210	18.082	18.531	81.830	

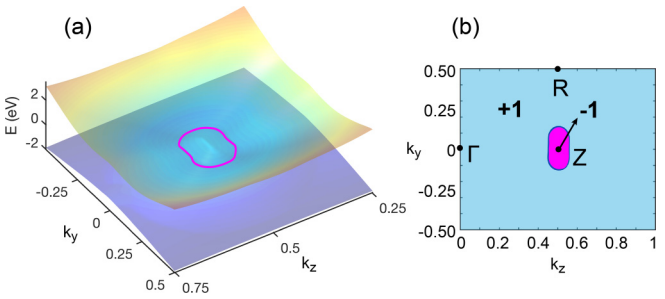

FIG. 6. (a) Energy dispersion of $P4_2/mbc$ phase at the $k_x = 0$ plane. The nodal loop is depicted by a magenta line and a dashed line. (b) Eigenvalues of the symmetry operation c-glide plane at the $k_x = 0$ plane.

$k_z = 0.5$ plane, this corresponds to four crossing points along the $\boldsymbol{b}_1$ and $\boldsymbol{b}_2$ directions, i.e., $(q_1, 0, 0.5)$ and $(0, q_2, 0.5)$, where $q_1^2 = -a_3/c_3$ and $q_2^2 = -a_3/d_3$. In the $k_x = 0$ and $k_y = 0$ planes, this corresponds to two degenerate nodal loops. The nodal loops are described by elliptic equations. These are $d_3k_y^2 + e_3\tilde{k}_z^2 + b_3\tilde{k}_z + a_3 = 0$ in the $k_x = 0$ plane and $c_3k_x^2 + e_3\tilde{k}_z^2 + b_3\tilde{k}_z + a_3 = 0$ in the $k_y = 0$ plane.

The model parameters are fitted from first-principles results and listed in Table I. The locations of crossing points determined by our effective Hamiltonian are $(\pm 0.13, 0, 0.5)$ and $(0, \pm 0.13, 0.5)$, which are consistent with our previous observation.

The existence of nodal loops can be further confirmed by symmetry analysis. Taking the $k_x = 0$ plane as an example, the nodal loop can be viewed from both the 3D energy dispersion [Fig. 6(a)] and the two-dimensional Brillouin plane [Fig. 6(b)]. The calculated eigenvalues of the c-glide plane are shown in Fig. 6(b). As the areas divided by the nodal loop (magenta) possess opposite eigenvalues with respect to c-glide plane with the area outside the nodal loop (blue), there must be band crossings on the boundary. This necessarily leads to degeneracy along nodal lines, which in this case are closed loops.

It should be remarked that recently developed topological quantum chemistry links the crystal symmetries of a given material with its topological properties [53]. Our further calculations based on this theory show that the electronic bands of these phases do not satisfy the compatibility relations, thus they are indeed to be classified as topological semimetals [54,55]. Interestingly, although the spin-orbit coupling is rather small for light elements such as lithium, the spin-orbit effects will open small gaps (about meV) for the *Cmca*-24 and *Cmca*-56 phases and turn them into three-dimensional strong topological insulators, while the $P4_2/mbc$ phase remains a topological semimetal.

IV. CONCLUSIONS

In computations on elemental Li at intermediate pressures of 200–360 GPa we find an electronic structure characteristic of a semimetal, with a low but nonvanishing density of states at the Fermi level. Detailed examination of the three competitive structural types in this region shows nodal loops in the band structure of each, centered at the Brillouin zones or at the boundaries of the Brillouin zones. The energies of these nodal loops are near the Fermi level. All these features can be characterized by $\boldsymbol{k} \cdot \boldsymbol{p}$ effective Hamiltonians constructed by us, based on symmetry analysis of the systems. In this pressure range elemental Li is computed to be a topological nodal-loop semimetal.

Nodal-loop semimetals have been predicted to host interesting properties, such as anisotropic electron transport and density fluctuations [56,57], unusual optical response and circular dichroism [58,59], and correlation effects and quantum oscillations [60]. Here, the nodal loops we predict in lithium under high pressure are rather simple and close to the Fermi level. These can serve as potential probes for identifying the predicted topological semimetallic nature of dense lithium experimentally.

Note added. Recently, we learned that Mack *et al.* [61] have also found topological features in lithium in the same phases and at roughly the same pressure range as in the present work.

ACKNOWLEDGMENTS

We thank Max Amsler for discussions and Prof. Neaton for communicating the work of Mack *et al.* [61] to us. This work was supported by the Energy Frontier Research in Extreme Environments (EFree) Center, an Energy Frontier Research Center funded by the U.S. Department of Energy, Office of Science under Award No. DE-SC0001057, and by LLNL. The work at LLNL was performed under the auspices of the U.S. DOE under Contract No. DE-AC52-07NA27344. J.F. and Z.Z. are supported by the MOST of the People's Republic of China (Grants No. 2018YFA0305601, and No. 2016YFA0301004), NSFC Grant No. 11725415, and by the Strategic Priority Research Program of Chinese Academy of Sciences, Grant No. XDB28000000.

S.F.E. and Z.Z. contributed equally to this work.

S.F.E., S.A.B., and R.H. designed the research. S.F.E. and Z.Z. performed the DFT calculations. Z.Z. and J.F. constructed the model Hamiltonian. All authors contributed to the data analysis and manuscript preparation.

The authors declare no competing financial interests.

[1] N. W. Ashcroft, Phys. Rev. B **39**, 10552 (1989).

[2] J. B. Neaton and N. W. Ashcroft, Nature (London) **400**, 141 (1999).

[3] E. Gregoryanz, O. Degtyareva, M. Somayazulu, R. J. Hemley, and H.-k. Mao, Phys. Rev. Lett. **94**, 185502 (2005).

[4] J. Tuoriniemi, K. Juntunen-Nurmilaukas, J. Uusvuori, E. Pentti, A. Salmela, and A. Sebedash, Nature (London) **447**, 187 (2007).

[5] J.-Y. Raty, E. Schwegler, and S. A. Bonev, Nature (London) **449**, 448 (2007).

[6] I. Tamblyn, J.-Y. Raty, and S. A. Bonev, Phys. Rev. Lett. **101**, 075703 (2008).

[7] T. Matsuoka and K. Shimizu, Nature (London) **458**, 186 (2009).

[8] Y. Ma, M. I. Eremets, A. R. Oganov, Y. Xie, I. A. Trojan, S. A. Medvedev, A. O. Lyakhov, M. Valle, and V. B. Prakapenka, Nature (London) **458**, 182 (2009).

[9] A. Lazicki and Y. Fei, Solid State Commun. **150**, 625 (2010).

[10] C. L. Guillaume, E. Gregoryanz, O. Degtyareva, M. I. McMahon, M. Hanfland, S. Evans, M. Guthrie, S. V. Sinogeikin, and H.-K. Mao, Nat. Phys. **7**, 211 (2011).

[11] F. A. Gorelli, S. F. Elatresh, C. L. Guillaume, M. Marqués, G. J. Ackland, M. Santoro, S. A. Bonev, and E. Gregoryanz, Phys. Rev. Lett. **108**, 055501 (2012).

[12] S. F. Elatresh, W. Cai, N. W. Ashcroft, R. Hoffmann, S. Deemyad, and S. A. Bonev, Proc. Natl. Acad. Sci. USA **114**, 5389 (2017).

[13] M. Hanfland, K. Syassen, N. E. Christensen, and D. L. Novikov, Nature (London) **408**, 174 (2000).

[14] C. J. Pickard and R. J. Needs, Phys. Rev. Lett. **102**, 146401 (2009).

[15] Anne Marie J. Schaeffer, W. B. Talmadge, S. R. Temple, and S. Deemyad, Phys. Rev. Lett. **109**, 185702 (2012).

[16] S. F. Elatresh, S. A. Bonev, E. Gregoryanz, and N. W. Ashcroft, Phys. Rev. B **94**, 104107 (2016).

[17] T. Matsuoka, M. Sakata, Y. Nakamoto, K. Takahama, K. Ichimaru, K. Mukai, K. Ohta, N. Hirao, Y. Ohishi, and K. Shimizu, Phys. Rev. B **89**, 144103 (2014).

[18] I. I. Naumov, R. J. Hemley, R. Hoffmann, and N. W. Ashcroft, J. Chem. Phys. **143**, 064702 (2015).

[19] Z. Yu, H. Y. Geng, Y. Sun, and Y. Chen, Sci. Rep. **8**, 3868 (2018).

[20] N. E. Christensen and D. L. Novikov, Phys. Rev. Lett. **86**, 1861 (2001).

[21] K. Shimizu, H. Ishikawa, D. Takao, T. Yagi, and K. Amaya, Nature (London) **419**, 597 (2002).

[22] N. W. Ashcroft, Nature (London) **419**, 569 (2002).

[23] V. V. Struzhkin, M. I. Eremets, W. Gan, H.-k. Mao, and R. J. Hemley, Science **298**, 1213 (2002).

[24] T. Matsuoka, S. Onoda, M. Kaneshige, Y. Nakamoto, K. Shimizu, T. Kagayama, and Y. Ohishi, J. Phys.: Conf. Ser. **121**, 052003 (2008).

[25] T. Bazhirov, J. Noffsinger, and M. L. Cohen, Phys. Rev. B **82**, 184509 (2010).

[26] S.-Y. Yue, L. Cheng, B. Liao, and M. Hu, Phys. Chem. Chem. Phys. **20**, 27125 (2018).

[27] J. Lv, Y. Wang, L. Zhu, and Y. Ma, Phys. Rev. Lett. **106**, 015503 (2011).

[28] B. Rousseau, Y. Xie, Y. Ma, and A. Bergara, Eur. Phys. J. B **81**, 1 (2011).

[29] M.-S. Miao and R. Hoffmann, Acc. Chem. Res. **47**, 1311 (2014).

[30] X. Wan, A. M. Turner, A. Vishwanath, and S. Y. Savrasov, Phys. Rev. B **83**, 205101 (2011).

[31] Z. Wang, Y. Sun, X.-Q. Chen, C. Franchini, G. Xu, H. Weng, X. Dai, and Z. Fang, Phys. Rev. B **85**, 195320 (2012).

[32] Z. Wang, H. Weng, Q. Wu, X. Dai, and Z. Fang, Phys. Rev. B **88**, 125427 (2013).

[33] Z. K. Liu, B. Zhou, Y. Zhang, Z. J. Wang, H. M. Weng, D. Prabhakaran, S.-K. Mo, Z. X. Shen, Z. Fang, X. Dai *et al.*, Science **343**, 864 (2014).

[34] S.-Y. Xu, I. Belopolski, N. Alidoust, M. Neupane, G. Bian, C. Zhang, R. Sankar, G. Chang, Z. Yuan, C.-C. Lee *et al.*, Science **349**, 613 (2015).

[35] S. Guan, Z.-M. Yu, Y. Liu, G.-B. Liu, L. Dong, Y. Lu, Y. Yao, and S. A. Yang, npj Quant. Mater. **2**, 23 (2017).

[36] S. Li, Y. Liu, B. Fu, Z.-M. Yu, S. A. Yang, and Y. Yao, Phys. Rev. B **97**, 245148 (2018).

[37] J. Hooper and E. Zurek, ChemPlusChem **77**, 969 (2012).

[38] I. I. Naumov and R. J. Hemley, Phys. Rev. Lett. **117**, 206403 (2016).

[39] C.-Z. Xu, Y.-H. Chan, Y. Chen, P. Chen, X. Wang, C. Dejoie, M.-H. Wong, J. A. Hlevyack, H. Ryu, H.-Y. Kee *et al.*, Phys. Rev. Lett. **118**, 146402 (2017).

[40] X. Gonze, B. Amadon, P.-M. Anglade, J.-M. Beuken, F. Bottin, P. Boulanger, F. Bruneval, D. Caliste, R. Caracas, M. Côté *et al.*, Comput. Phys. Commun. **180**, 2582 (2009).

[41] C. Hartwigsen, S. Goedecker, and J. Hutter, Phys. Rev. B **58**, 3641 (1998).

[42] J. P. Perdew, K. Burke, and M. Ernzerhof, Phys. Rev. Lett. **77**, 3865 (1996).

[43] G. Kresse and J. Furthmüller, Phys. Rev. B **54**, 11169 (1996).

[44] A. A. Mostofi, J. R. Yates, G. Pizzi, Y.-S. Lee, I. Souza, D. Vanderbilt, and N. Marzari, Comput. Phys. Commun. **185**, 2309 (2014)

[45] Y. Ma, A. R. Oganov, and Y. Xie, Phys. Rev. B **78**, 014102 (2008).

[46] J. Heyd, G. E. Scuseria, and M. Ernzerhof, J. Chem. Phys. **124**, 219906 (2006).

[47] G. Kresse and J. Hafner, Phys. Rev. B **47**, 558 (1993).

[48] N. Marzari and D. Vanderbilt, Phys. Rev. B **56**, 12847 (1997).

[49] J. Feng, R. G. Hennig, N. W. Ashcroft, and R. Hoffmann, Nature (London) **451**, 445 (2008).

[50] See Supplemental Material at http://link.aps.org/supplemental/10.1103/PhysRevMaterials.3.044203 for additional theoretical details and analysis for the difference between Cmca-24 and Pbca phases.

[51] J. L. Dye, Science **301**, 607 (2003).

[52] Y. X. Zhao, A. P. Schnyder, and Z. D. Wang, Phys. Rev. Lett. **116**, 156402 (2016).

[53] B. Bradlyn, L. Elcoro, J. Cano, M. G. Vergniory, Z. Wang, C. Felser, M. I. Aroyo, and B. A. Bernevig, Nature (London) **547**, 298 (2017).

[54] M. G. Vergniory, L. Elcoro, C. Felser, N. Regnault, B. A. Bernevig, and Z. Wang, Nature (London) **566**, 480 (2019).

[55] Z. Song, T. Zhang, and C. Fang, Phys. Rev. X **8**, 031069 (2018).

[56] K. Mullen, B. Uchoa, and D. T. Glatzhofer, Phys. Rev. Lett. **115**, 026403 (2015).

[57] J.-W. Rhim and Y. B. Kim, New J. Phys. **18**, 043010 (2016).

[58] J. P. Carbotte, J. Phys.: Condens. Matter **29**, 045301 (2016).

[59] Y. Liu, S. A. Yang, and F. Zhang, Phys. Rev. B **97**, 035153 (2018).

[60] J. Liu and L. Balents, Phys. Rev. B **95**, 075426 (2017).

[61] S. A. Mack, S. M. Griffin, and J. B. Neaton, arXiv:1904.01248.